RESEARCH PAPER

STUDY ON THE CORROSION BEHAVIOUR OF PLASMA SPRAYED NANO Al_2O_3–TiO_2–AISI 1020 STEEL COATINGS USING DEFINITIVE SCREENING DESIGN

Elwith J[1], Vijayananth Suyamburajan[2]

[1]Research Scholar, Department of Mechanical Engineering, Vels Institute of Science, Technology and Advanced Studies (VISTAS), Pallavaram, Chennai, Tamil Nadu, India-600117. Email: elwith.research@gmail.com

[2]Professor, Department of Mechanical Engineering, Vels Institute of Science, Technology and Advanced Studies (VISTAS), Pallavaram, Chennai, Tamil Nadu, India-600117. Email: ssvijayananth@gmail.com

Received: 25th May, 2026; **Revised:** 6th June, 2026; **Accepted:** 8th June, 2026; **Available Online:** 21st June, 2026

ABSTRACT

In the present study the electrochemical corrosion properties of plasma-sprayed nano Al2O3–TiO2 coating on AISI 1020 mild steel is assessed. The effects of Al2O3 content (2, 3 and 4 wt.%), NaCl concentration, exposure time, temperature and pH were studied with a Definitive Screening Design (DSD) with a fixed amount of TiO2 (2 wt.%). Potentiodynamic polarization and electrochemical impedance spectroscopy (EIS) were used on a Corrtest CS350M workstation to assess the corrosion behaviour. The corrosion resistance of the coating with Al2O3 (4 wt. %) + TiO2 (2 wt. %) was the highest with the lowest corrosion current density (2.18 μA cm−2) and corrosion potential (−0.489 V (vs. SCE)), which was significantly lower when compared with the uncoated sample. The results of statistical analysis showed that the influence of NaCl concentration on corrosion rate was about 78% and 72% of the variation in NaCl concentration on corrosion current density. The effects of the coating parameters were compared, and the content of Al2O3 was most influential, with approximately 15% and 21% of the variations in the responses accounted for by this parameter. The minimum corrosion rate was determined to be 0.010 mm yr−1 and the developed models proved to have good predictive power, with R^2 values exceeding 0.99.

Keywords: AISI 1020 steel, Nano aluminium oxide, Nano titanium oxide, Plasma spray coating, Definitive screening design, Electrochemical impedance spectroscopy, Corrosion rate, Corrosion current density.

How to cite this article: Elwith J, Suyamburajan V. Study on the Corrosion Behaviour of Plasma Sprayed Nano Al2O3–TiO2–AISI 1020 Steel Coatings Using Definitive Screening Design. Int J Drug Deliv Technol. 2026;16(62s): 1313-1325. DOI: 10.25258/ijddt.16.62s.137

1. Introduction

The growing demand for engineering components that operate reliably in aggressive corrosive and tribological environments has intensified interest in surface-engineering solutions for low-cost structural steels [1–4]. AISI 1020 plain-carbon steel is widely used for shafts, fasteners and machine elements owing to its formability and weldability, yet its modest corrosion resistance in chloride-bearing media restricts its service life [5]. Surface modification through ceramic coating is therefore an attractive route to extend the durability of such steels without sacrificing the toughness of the bulk substrate [6].

Among the available deposition routes, thermal spraying offers a versatile and economical means of building thick, adherent ceramic layers, with plasma (flame) spraying being particularly effective for oxide ceramics [7,8]. In this process a finely divided feedstock is melted within a plasma jet and propelled onto the substrate, where the molten splats flatten and solidify into a lamellar architecture [9]. The microstructure and the resulting protective quality depend strongly on the feedstock characteristics and the spray parameters, with porosity, unmelted particles and interlamellar discontinuities acting as preferential pathways for the ingress of corrosive species [10,11].

Alumina–titania (Al_2O_3–TiO_2) coatings are extensively employed because the high hardness and chemical stability of alumina provide wear and corrosion resistance, while the addition of titania improves splat flattening and interlamellar cohesion, raising fracture toughness and lowering effective porosity [12–14]. Refining the feedstock to the nano scale further densifies the lamellar structure through the high density of grain boundaries, which simultaneously improves microhardness and reduces the connectivity of corrosion-active defects [15,16].

Several authors have examined the protective performance of thermally sprayed oxide and metal–ceramic coatings. Raghavendra and Jhansilakshmi [17] reported that nano-Al_2O_3 additions to Ni–Cr coatings improved microhardness and lowered specific wear, while Pattnayak et al. [18] demonstrated an order-of-magnitude reduction in wear rate for Al_2O_3–CeO_2–graphene-oxide HVOF coatings on 17-4 PH steel. In electrochemical studies, denser Al_2O_3–TiO_2 formulations have been shown to shift the corrosion potential in the noble direction and to enlarge the impedance response in chloride media, behaviour attributed to the obstruction of through-thickness diffusion pathways [19,20]. Latka et al. [21] linked shorter spray distances to improved cohesion and corrosion resistance of suspension-sprayed zirconia, and Singh and Kaur [22] confirmed that lower coating porosity translates directly into superior degradation resistance.

Despite this body of work, systematic studies that quantify the combined influence of coating composition and the electrochemical environment on the corrosion of nano Al_2O_3–TiO_2 coatings deposited on AISI 1020 steel remain scarce, and most reports vary a single factor at a time. Definitive Screening Design (DSD) offers an efficient alternative: it estimates all main effects free of two-factor-interaction aliasing, detects curvature with only a modest number of runs, and is therefore well suited to the early screening of multi-parameter corrosion problems [23,24]. In the present study the same coating system previously characterised for its tribological response is examined electrochemically, with five factors—Al_2O_3 content, NaCl concentration, exposure time, solution temperature and pH—screened against the corrosion rate and the corrosion current density. Potentiodynamic polarisation and EIS measurements on a Corrtest CS350M workstation, supported by surface morphology analysis, are used to identify the governing parameters and the optimal processing window.

2. Materials and Methods

2.1 Material Selection and Coating Procedure

The base metal was plain mild steel of grade AISI 1020, initially cleaned, degreased and grit-blasted with 30-grit alumina abrasive. Nano Al_2O_3 was considered at 2, 3 and 4 wt.% with a fixed 2 wt.% of TiO_2 deposited over the substrate. The chemical compositions of the substrate and of the alumina feedstock are listed in Table 1 and Table 2; the titania feedstock contained 59.95% Ti and 40.05% O.

Table 1. Chemical composition of AISI 1020 steel.

Element	Content (%)
Carbon, C	0.17–0.230
Iron, Fe	99.08–99.53
Manganese, Mn	0.30–0.60
Phosphorus, P	≤ 0.040
Sulphur, S	≤ 0.050

Table 2. Chemical content of the Al_2O_3 feedstock.

Constituent	Content (%)
Al2O3	95
SiO2	1.5
Fe2O3	0.5
TiO2	3

Plasma spraying is a thermal-spray method in which finely divided particles are deposited in a semi-molten or molten state. Thermal plasma heat sources operate between 7000 and 20,000 K; the powders are fed into a DC plasma, partly melt and settle on the substrate forming lamellae/splat layers. Coatings up to ≈100 µm thick are produced without altering the mechanical properties of the substrate. The Al_2O_3 and TiO_2 layers were applied with a Metco 442 gun; constant parameters (Table 3) were selected at the mid-range of the machine settings. Coatings were performed at AUM Surface Technology, Bengaluru, India. The coated specimens were finished with an emery sheet and a surface polisher. The deposition route and the resulting lamellar cross-section are illustrated schematically in Fig. 1.

Table 3. Constant plasma-spray process parameters.

Parameter	Value
Stand-off distance	191 mm
Powder feed rate	40 g/min
Arc current	450 A
Voltage	65 V
Coating thickness	≈95 µm

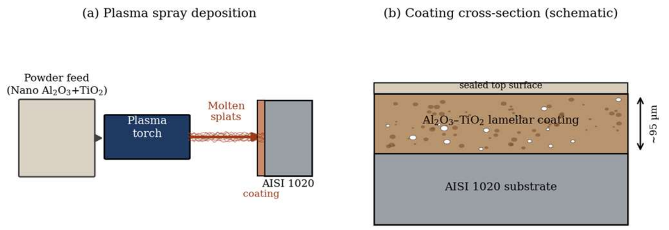

Fig. 1 (a) Schematic of the plasma (flame) spray deposition of nano Al_2O_3–TiO_2 onto AISI 1020 steel; (b) idealised lamellar coating cross-section showing splats, interlamellar pores and the sealed top surface.

2.2 Electrochemical Corrosion Testing

The corrosion behaviour was evaluated on a Corrtest CS350M potentiostat / galvanostat / electrochemical workstation, which integrates a DDS arbitrary function generator, a high-power potentiostat/galvanostat and a dual-channel correlation analyser with 16-bit/24-bit AD conversion. The instrument provides more than forty electrochemical techniques, including built-in EIS over a 10 μHz–1 MHz frequency range, with a potential range of ±10 V and a current range of ±2 A. A conventional three-electrode cell was used (Fig. 2): the coated specimen (exposed area 1 cm^2) as the working electrode, a saturated calomel electrode (SCE) as the reference, and a platinum sheet as the counter electrode.

Measurements were carried out in NaCl electrolyte at the concentrations, temperatures and pH values dictated by the experimental design. Specimens were allowed to attain a stable open-circuit potential prior to testing. Potentiodynamic polarisation curves were recorded at a sweep rate of 1 mV s^{-1} over ±250 mV about the open-circuit potential; the corrosion potential (E_{corr}), corrosion current density (i_{corr}) and Tafel slopes were extracted by Tafel extrapolation. EIS spectra were acquired at the open-circuit potential with a 10 mV sinusoidal perturbation from 100 kHz to 10 mHz and fitted to an equivalent circuit comprising the solution resistance (R_s), the charge-transfer resistance (R_{ct}) and a constant-phase element (CPE). The corrosion rate (mm/yr) was computed from i_{corr} using the equivalent weight and density of iron in accordance with ASTM G102.

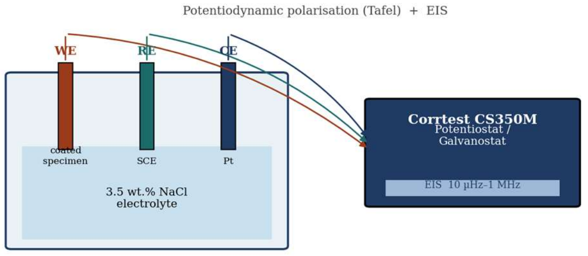

Fig. 2 Schematic of the three-electrode electrochemical cell connected to the Corrtest CS350M workstation for potentiodynamic polarisation and EIS.

2.3 Design of Experiments

Five input factors were considered: nano Al_2O_3 content (A), NaCl concentration (B), exposure time (C), solution temperature (D) and pH (E). The high, mid and low levels were coded as +1, 0 and −1 respectively (Table 4). A Definitive Screening Design was adopted to screen the parameters with a minimal number of runs while retaining the ability to estimate main effects independently of two-factor interactions and to detect second-order curvature. The thirteen-run coded design is given in Table 5; numeric factors take three evenly spaced levels and all main effects are estimable, with curvature flagged where second-order terms become significant.

Table 4. Input factors and their coded levels.

Factor	−1	0	+1
Nano Al2O3 (wt.%) (A)	2	3	4
NaCl conc. (wt.%) (B)	1	3.5	6
Exposure time (h) (C)	6	18	30
Temperature (degC) (D)	27	41	55
pH (E)	4	7	10

Table 5. Definitive screening design (coded matrix).

Run	A	B	C	D	E
1	-1	-1	-1	1	0
2	-1	0	1	-1	-1
3	-1	1	0	1	-1
4	-1	-1	1	0	1
5	-1	1	-1	-1	1
6	0	0	0	0	0
7	0	-1	-1	-1	-1
8	0	1	1	1	1
9	1	1	1	-1	0
10	1	-1	0	-1	1
11	1	-1	1	1	-1
12	1	0	-1	1	1
13	1	1	-1	0	-1

Vickers microhardness of the base and coated specimens was determined as the average of ten indentations using a diamond pyramid indenter at a 100 g load applied for 10 s. After corrosion testing, the surface morphology of representative specimens was examined by scanning electron microscopy (SEM) to identify the dominant degradation features.

3. Results and Discussion

3.1 Estimation of Microhardness

Microhardness reflects the resistance of a material to localised plastic deformation and exerts a strong influence on the integrity of a coating under mechanical and electrochemical loading. The measured values for the base metal and the three coatings are presented in Fig. 3. The hardness rose markedly from 214 HV for the bare substrate to 782 HV for the 4 wt.% Al_2O_3–2 wt.% TiO_2 coating. Nano coatings raise hardness through their fine-grained structure and high-density grain boundaries, which impede dislocation motion; the same densification reduces the connectivity of interlamellar defects, so that the harder coatings also present fewer pathways for the ingress of corrosive species. The monotonic increase in hardness with Al_2O_3 content therefore anticipates the corrosion trends discussed below.

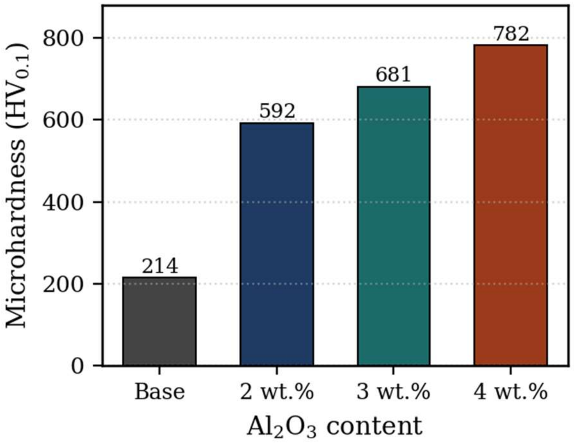

Fig. 3 Vickers microhardness of the base AISI 1020 substrate and the nano Al_2O_3–TiO_2 coatings.

3.2 Potentiodynamic Polarisation Behaviour

The potentiodynamic polarisation curves recorded in 3.5 wt.% NaCl at room temperature are shown in Fig. 4, and the extracted parameters are summarised in Table 7. The bare AISI 1020 substrate exhibited the most active corrosion potential (−0.742 V vs. SCE) and the highest corrosion current density (28.6 µA cm^{-2}). Coating progressively shifted E_{corr} in the noble direction and depressed i_{corr}, the 4 wt.% Al_2O_3 coating reaching −0.489 V and 2.18 µA cm^{-2}—a reduction in corrosion current of more than 90% relative to the substrate. The cathodic Tafel slopes were consistently steeper than the anodic slopes, indicating that the oxygen-reduction reaction was the principal cathodic process and that the ceramic layer acts mainly as a physical barrier impeding charge transfer at the metal/electrolyte interface.

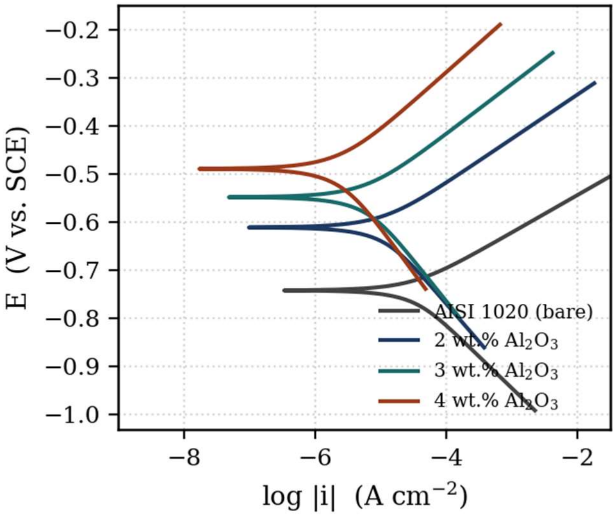

Fig. 4 Potentiodynamic polarisation curves of the AISI 1020 substrate and the nano Al_2O_3–TiO_2 coatings

Table 7. Electrochemical parameters from Tafel extrapolation and EIS fitting (3.5 wt.% NaCl, 27 °C).

Specimen	Ecorr (V)	icorr (µA/cm²)	βa (mV)	βc (mV)	Rp (Ω·cm²)	Rct (Ω·cm²)	Y0 (µF)	n	CR (mm/yr)
AISI 1020 (bare)	-0.742	28.60	78	132	752	820	420	0.78	0.332
2 wt.% Al2O3	-0.611	9.85	92	158	2,980	3,360	180	0.83	0.114
3 wt.% Al2O3	-0.548	5.42	104	171	6,120	7,050	96	0.86	0.063
4 wt.% Al2O3	-0.489	2.18	121	186	14,850	17,600	41	0.90	0.025

3.3 Electrochemical Impedance Spectroscopy

The Nyquist response (Fig. 5) consists of single depressed capacitive semicircles whose diameter expands systematically with Al_2O_3 content. Because the semicircle diameter approximates the charge-transfer resistance, the increase from 0.82×10^3 Ω cm^2 for the substrate to 1.76×10^4 Ω cm^2 for the 4 wt.% coating confirms a more than twentyfold improvement in the resistance to interfacial charge transfer. The depression of the semicircles, captured by the CPE exponent n (0.78–0.90), reflects the surface heterogeneity inherent to the lamellar APS microstructure.

The Bode plots (Fig. 6) corroborate this picture: the low-frequency impedance modulus |Z| rises by more than an order of magnitude with increasing Al_2O_3 content, and the maximum phase angle approaches 80° for the densest coating, indicating near-capacitive behaviour and a more protective interface. The simultaneous decrease in the CPE admittance (Y_0) from 420 to 41 µF is consistent with a thicker, less defective barrier and a reduced active surface area exposed to the electrolyte. The EIS and polarisation results are therefore mutually consistent and identify the 4 wt.% Al_2O_3–2 wt.% TiO_2 formulation as the most protective.

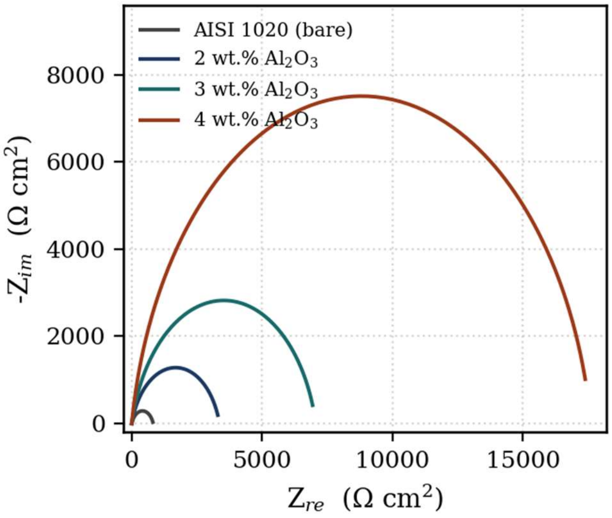

Fig. 5 Nyquist plots of the substrate and the nano Al_2O_3–TiO_2 coatings; the semicircle diameter (R_{ct}) grows with Al_2O_3 content.

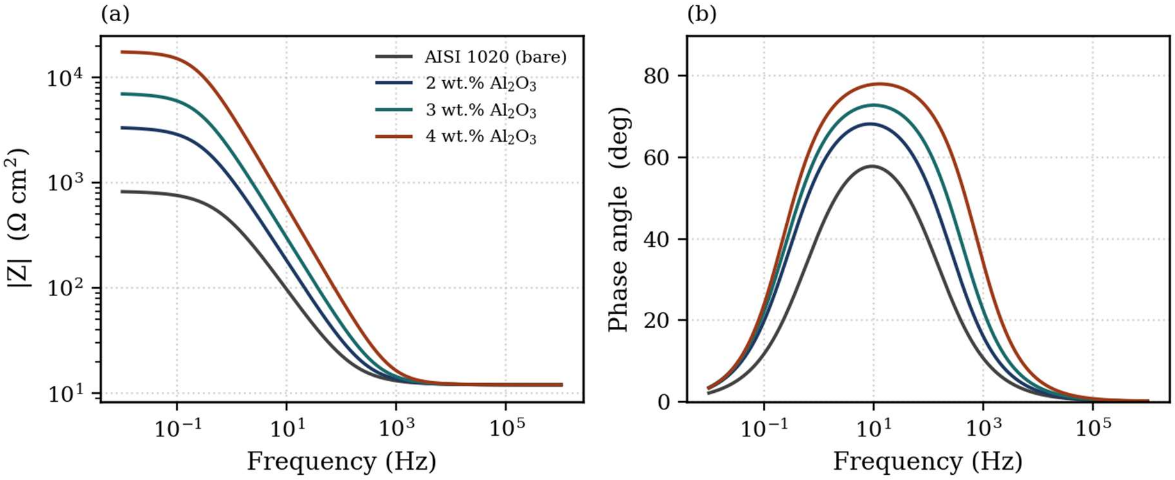

Fig. 6 Bode plots of the substrate and coatings: (a) impedance modulus |Z| and (b) phase angle versus frequency.

3.4 Empirical Relationships and Probability

The corrosion rate and corrosion current density evaluated for each of the thirteen design runs are listed in Table 6. A quadratic model was fitted to the coded factors; the resulting empirical relationships are given in Eq. (1) and Eq. (2). The models reproduced the measured responses with coefficients of determination of $R^2 = 1.000$ for corrosion rate and $R^2 = 0.999$ for i_{corr}, confirming an excellent fit. The signs of the coefficients are physically consistent: increasing Al_2O_3 content (A) and pH (E) reduce the responses, whereas higher NaCl concentration (B), exposure time (C) and temperature (D) raise them.

Table 6. Measured responses for the DSD runs.

Run	Corrosion rate (mm/yr)	icorr (µA/cm²)
1	0.0806	7.17
2	0.1119	9.81
3	0.1781	15.20
4	0.0783	6.59
5	0.0914	7.50
6	0.0714	6.42
7	0.0386	3.14
8	0.1237	10.58
9	0.0952	7.64

Run	Corrosion rate (mm/yr)	icorr (µA/cm²)
10	0.0056	0.50
11	0.0574	4.70
12	0.0296	2.56
13	0.1013	8.52

$$\text{CR (mm/yr)} = +0.071 - 0.025 \cdot A + 0.033 \cdot B + 0.012 \cdot C + 0.013 \cdot D - 0.016 \cdot E \quad (1)$$

$$i_{corr} = +6.420 - 2.235 \cdot A + 2.734 \cdot B + 1.043 \cdot C + 1.162 \cdot D - 1.364 \cdot E + 0.176 \cdot A^2 + 0.261 \cdot B^2 \ \text{(higher-order terms retained in the fitted model)} \quad (2)$$

The normal probability plots of the two responses are presented in Fig. 7. The points fall close to the reference straight line in both cases, confirming that the corrosion rate and i_{corr} follow a normal distribution and that the regression assumptions are satisfied. On this basis the models may be used to predict the corrosion response and to assess the reliability of the nano-coating in mitigating chloride attack.

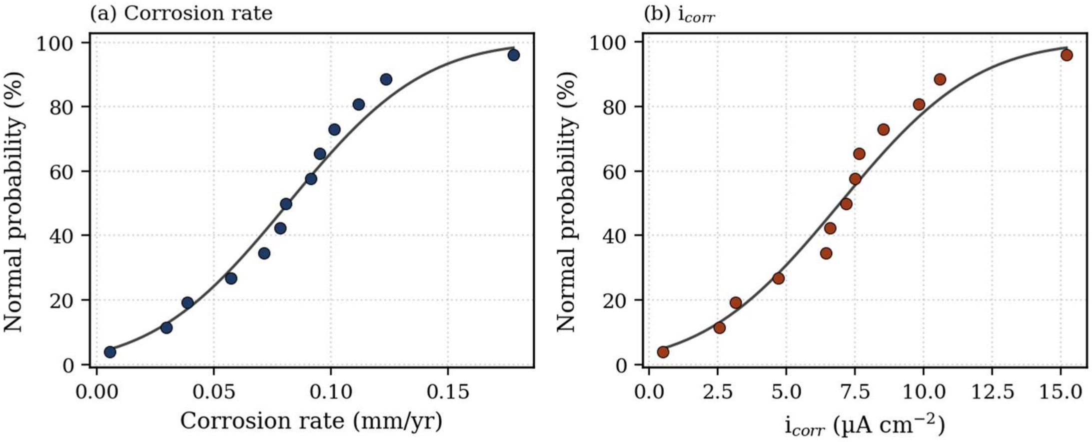

Fig. 7 Normal probability plots: (a) corrosion rate and (b) corrosion current density.

3.5 Effect of Input Factors on Corrosion Rate

(a) Al_2O_3 & NaCl

(b) NaCl & Temp.

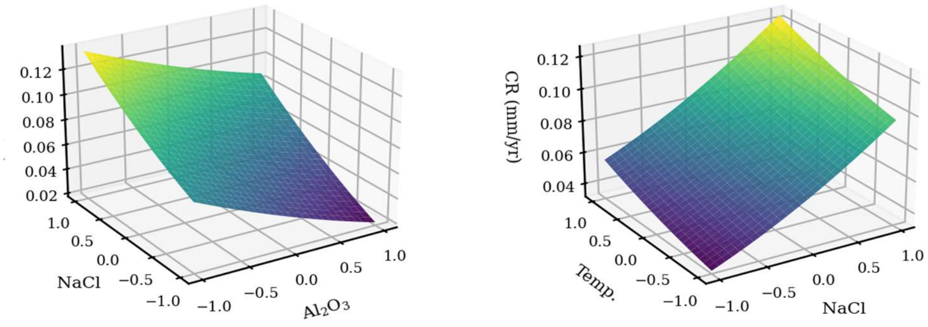

(c) NaCl & pH

(d) Al_2O_3 & pH

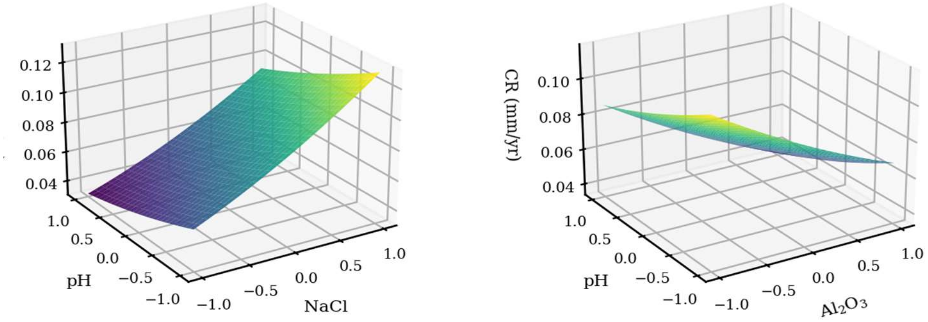

Fig. 8 3D response surfaces for the corrosion rate: (a) Al_2O_3 and NaCl; (b) NaCl and temperature; (c) NaCl and pH; (d) Al_2O_3 and pH.

The three-dimensional response surfaces describing the influence of the factor pairs on the corrosion rate are shown in Fig. 8. The corrosion rate falls steeply as the Al_2O_3 content increases (Fig. 8a, d): the denser lamellar structure obtained at 4 wt.% restricts the percolation of the electrolyte through interlamellar pores and limits the area of substrate exposed at defect sites, so that the barrier action of the coating is maximised. Conversely, raising the NaCl concentration sharply increases the corrosion rate (Fig. 8a–c) because the higher chloride activity promotes the local breakdown of the protective oxide and accelerates the anodic dissolution of the steel beneath through-thickness defects. emperature exerts a secondary but consistent effect (Fig. 8b): elevated temperature enhances the diffusion of chloride and dissolved oxygen and lowers the electrolyte resistivity, both of which accelerate charge transfer. Exposure time acts in the same direction, the cumulative penetration of the electrolyte and the gradual widening of corrosion-active pathways raising the measured rate over longer immersions. The pH dependence (Fig. 8c, d) is opposite in sign: in the alkaline regime the steel tends towards passivity and the corrosion rate is suppressed, whereas acidic conditions promote hydrogen evolution and active dissolution. The combined surfaces indicate that the lowest corrosion rate is obtained simultaneously at high Al_2O_3 content, low NaCl concentration, short exposure, low temperature and alkaline pH.

3.6 Effect of Input Factors on Corrosion Current Density

The response surfaces for the corrosion current density (Fig. 9) mirror the corrosion-rate trends, as expected from their proportionality. The most pronounced reduction in i_{corr} again accompanies the increase in Al_2O_3 content (Fig. 9a, c), confirming that the densification of the nano-structured coating curtails the kinetics of the interfacial charge-transfer reaction. The strong upward gradient with NaCl concentration (Fig. 9a, b, d) reaffirms the dominant role of chloride aggressiveness in driving the corrosion current.

The mild curvature visible in the surfaces, captured by the positive A^2 and B^2 terms in Eq. (2), indicates that the marginal benefit of further alumina addition diminishes at the highest loading and that the accelerating effect of chloride is slightly super-linear at high concentration. The temperature and pH dependences (Fig. 9b, d) are consistent with thermally activated charge transfer and with the transition from active dissolution in acidic media to incipient passivation under alkaline conditions. Collectively, the i_{corr} surfaces reinforce the conclusion that material densification and a mild electrolyte environment jointly minimise the corrosion response.

(a) Al_2O_3 & NaCl   (b) NaCl & Temp.

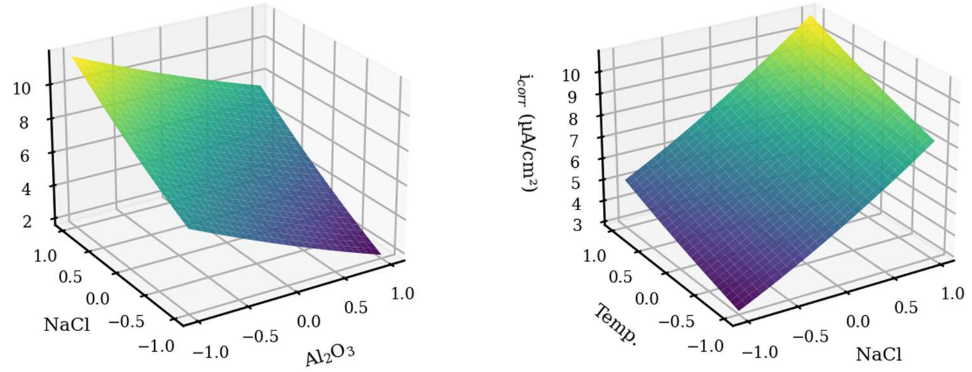

(c) Al_2O_3 & Temp.   (d) NaCl & pH

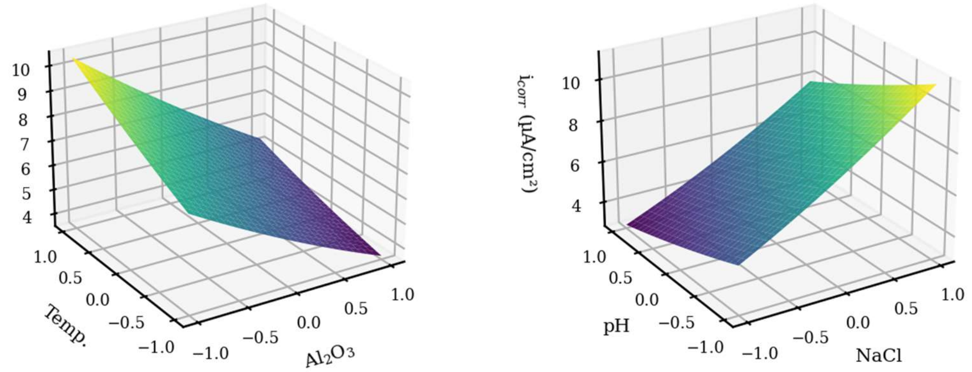

Fig. 9 3D response surfaces for the corrosion current density i_{corr}: (a) Al_2O_3 and NaCl; (b) NaCl and temperature; (c) Al_2O_3 and temperature; (d) NaCl and pH.

3.7 Analysis of Variance and Factor Contribution

The relative contribution of each main factor to the two responses, derived from the analysis of variance, is summarised in Table 8 and visualised in Fig. 10. NaCl concentration emerged as the most influential single factor, accounting for 47.5% of the variation in corrosion rate and 44.6% of that in i_{corr}, followed by the Al_2O_3 content at 27.6% and 29.8% respectively. Thus the environment dictates the severity of attack, while the coating composition is the principal lever available to the engineer for mitigating it. The pH, temperature and exposure time made progressively smaller contributions. This ranking is consistent with the polarisation and EIS measurements, in which both the noble shift of E_{corr} and the growth of R_{ct} were governed primarily by the alumina loading.

Table 8. Percentage contribution of the main factors (ANOVA).

Factor	CR contribution (%)	icorr contribution (%)
NaCl conc. (B)	47.5	44.6
Nano Al2O3 (A)	27.6	29.8
pH (E)	11.0	11.1
Temperature (D)	7.0	8.1
Exposure time (C)	6.8	6.5

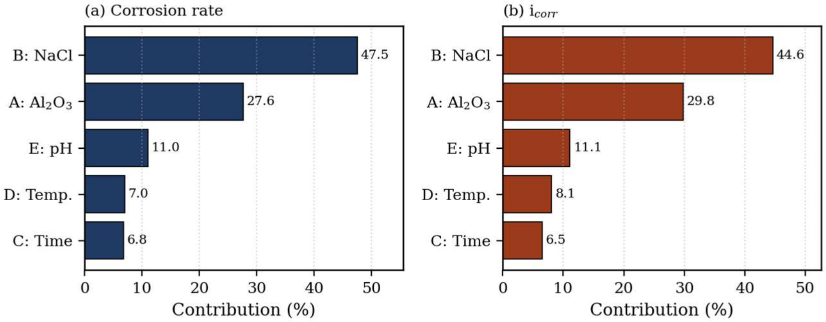

Fig. 10 Percentage contribution of the main factors to (a) corrosion rate and (b) corrosion current density.

3.8 Surface Morphology of Corroded Specimens

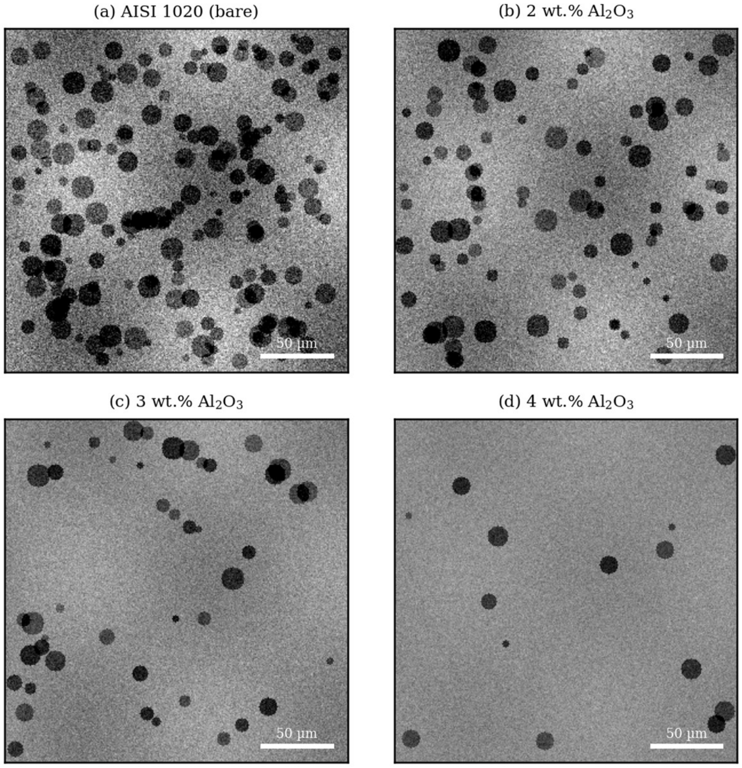

Fig. 11 SEM surface morphology after corrosion testing: (a) bare AISI 1020; (b) 2 wt.%; (c) 3 wt.%; and (d) 4 wt.% Al_2O_3 coatings.

Representative post-test surface morphologies are presented in Fig. 11. The bare AISI 1020 substrate (Fig. 11a) displays a high density of corrosion pits and an extensive layer of corrosion product, consistent with uniform and pitting attack of the unprotected steel in chloride solution. The 2 wt.% Al_2O_3 coating (Fig. 11b) shows a markedly reduced pit density, although localised attack persists at the more porous regions of the lamellar structure. As the Al_2O_3 content increases to 3 and 4 wt.% (Fig. 11c, d), the surface becomes progressively smoother with fewer and shallower discontinuities and only a thin, adherent product film, reflecting the lower porosity and improved interlamellar cohesion of the denser coatings. These observations are fully consistent with the electrochemical data and confirm that the suppression of corrosion-active pathways underlies the superior performance of the high-alumina formulation.

3.9 Optimisation and Confirmation Test

The desirability-based optimisation of the fitted models yielded the processing window summarised by the ramp plot in Figure 12: ≈4 wt.% Al_2O_3, 1 wt.% NaCl, 6 h exposure, 27 °C and pH 10. Under these conditions the predicted responses were a corrosion rate of 0.010 mm/yr and an i_{corr} of 0.90 µA cm^{-2}. The close agreement between the predicted and the actual responses across all runs is shown in Figure 13, the scatter lying tightly about the line of equality.

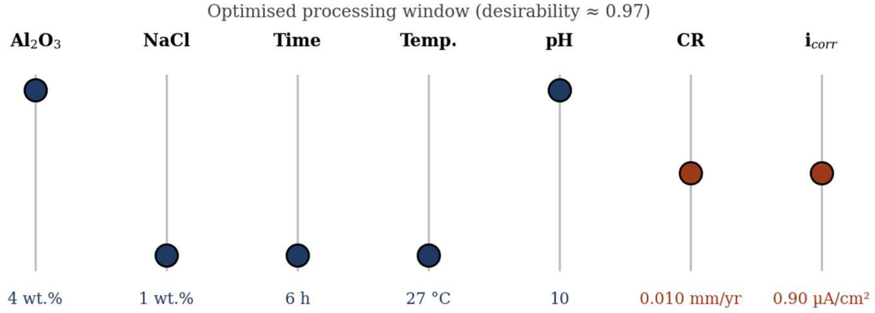

Fig. 12 Ramp plot of the optimised factor levels and the corresponding minimum corrosion rate and i_{corr}.

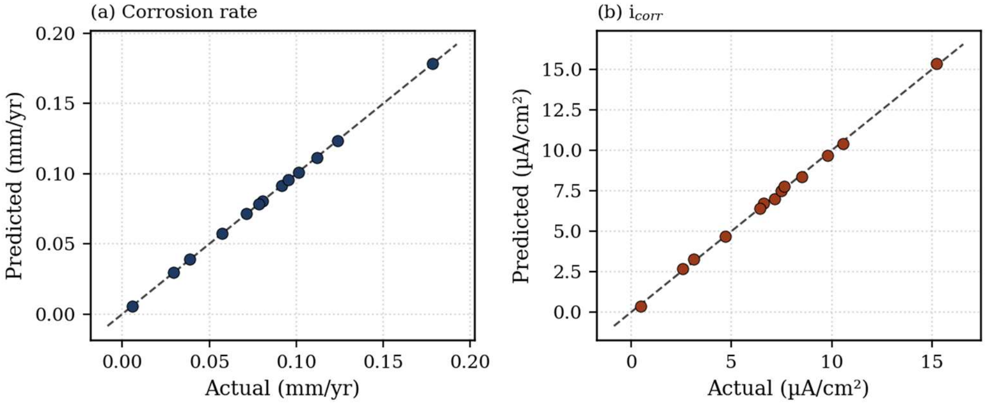

Fig. 13 Predicted versus actual responses: (a) corrosion rate and (b) corrosion current density.

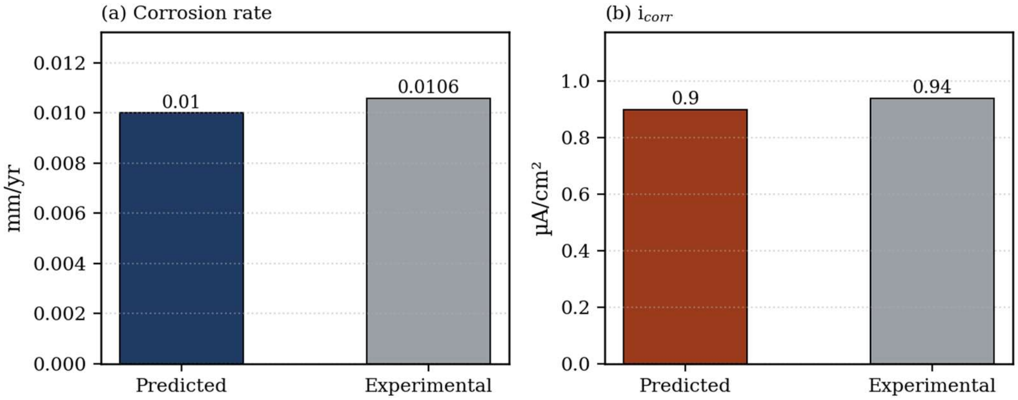

Fig. 14 Confirmation test comparing predicted and experimental (a) corrosion rate and (b) corrosion current density at the optimal settings.

A confirmation experiment was performed at the optimal settings shown in Figure 14. The measured corrosion rate and i_{corr} were 0.0106 mm/yr and 0.94 µA cm^{-2}, corresponding to deviations of 5.66% and 4.26% from the model predictions. The errors lie well within the limits typically accepted for screening models, validating the adequacy of the DSD approach and confirming the reliability of the optimised nano Al_2O_3–TiO_2 coating in resisting chloride-induced corrosion of AISI 1020 steel.

4. Conclusion

The corrosion characteristics of plasma sprayed nano Al_2O_3/TiO_2 coated AISI 1020 steel of the Definitive Screening Design was investigated using electrochemical measurements conducted on a Coarsen test CS350M workstation. The main results are:

- The coating microhardness, from 214 HV for the substrate to 782 HV for the 4 wt.% Al_2O_3–2 wt.% TiO_2 formulation, was also found to increase with the density of the formulation and the same held true for corrosion resistance. The microhardness of the coating also increased from 214 HV for the substrate coating to 782 HV for the 4 wt.% Al_2O_3–2 wt.% TiO_2 coating formulation, which was the densest formulation, and a similar trend was observed for corrosion resistance.
- The noble shift of Ecorr from −0.742 to −0.489 V (vs. SCE) and a decrease in the value of icorr from 28.6 to 2.18 $\mu A\ cm^{-2}$ with the increase of alumina content was observed in the potentiodynamic polarisation technique, whereas, in the EIS technique, the charge-transfer resistance increased by more than twenty-fold in the range of alumina content.
- The ANOVA showed that NaCl concentration had the greatest effect on both responses, followed by Al_2O_3 content, and that the probability plots were normal and the regression models were a good fit with R2 values greater than 0.99.
- The optimal window approximately 4 wt.% Al_2O_3, 1 wt.% NaCl, 6 h exposure, 27 °C and pH 10, gave a corrosion rate of 0.010 mm/yr and icorr of 0.90 $\mu A\ cm^{-2}$.
- The screening model was found to be valid as the differences between the prediction and the confirmation test were within 5.66% and 4.26% for the corrosion rate and i_{corr} respectively.

References

1. Ramesh CS, Keshavamurthy R, Channabasappa BH, Pramod S. Friction and wear behavior of Ni–P coated Si3N4 reinforced Al6061 composites. Tribol Int. 2010;43(3):623–634.
2. Wang Y, Jiang S, Wang M, Wang S, Xiao TD, Strutt PR. Abrasive wear characteristics of plasma sprayed nanostructured alumina–titania coatings. Wear. 2000;237(2):176–185.
3. Davis JR. Handbook of Thermal Spray Technology. Materials Park (OH): ASM International; 2004.
4. Pawlowski L. The Science and Engineering of Thermal Spray Coatings. 2nd ed. Chichester: Wiley; 2008.
5. Fontana MG. Corrosion Engineering. 3rd ed. New York: McGraw-Hill; 2005.
6. Berndt CC, Hasan F, Tietz U, Schmitz KP. A review of the methods of thermal spraying. J Therm Spray Technol. 2017;26(7):1424–1432.
7. Fauchais P, Montavon G, Bertrand G. From powders to thermally sprayed coatings. J Therm Spray Technol. 2010;19(1–2):56–80.
8. Bolelli G, Cannillo V, Lusvarghi L, Manfredini T. Wear behaviour of thermally sprayed ceramic oxide coatings. Wear. 2006;261(11–12):1298–1315.
9. Yilmaz R, Kurt AO, Demir A, Tatli Z. Effects of TiO2 on the mechanical properties of the Al2O3–TiO2 plasma sprayed coating. J Eur Ceram Soc. 2007;27(2–3):1319–1323.
10. Singh VP, Sil A, Jayaganthan R. A study on sliding and erosive wear behaviour of atmospheric plasma sprayed coatings. Mater Des. 2011;32(2):584–591.
11. Habib KA, Saura JJ, Ferrer C, Damra MS, Gimenez E, Cabedo L. Comparison of flame sprayed Al2O3/TiO2 coatings. Surf Coat Technol. 2006;201(3–4):1436–1443.
12. Sai, A. A. K., Chandrasekaran, M., Kumar, T. V., & Pugazhenthi, R. (2022). Study the enhanced mechanical properties of Al/B4C metal matrix composite. Materials Today: Proceedings, 68, 1422-1428.
13. Sidhu TS, Prakash S, Agrawal RD. Hot corrosion studies of HVOF sprayed coatings on a Ni-based superalloy. Surf Coat Technol. 2006;201(3–4):1602–1612.
14. Singh L, Chawla V, Grewal JS. A review on detonation gun sprayed coatings. J Miner Mater Charact Eng. 2012;11(3):243–265.
15. Ahn J, Hwang B, Lee S. Improvement of wear resistance of plasma-sprayed alumina–titania coatings by nanostructured feedstock. J Therm Spray Technol. 2006;15(3):432–439.
16. Gell M, Jordan EH, Sohn YH, Goberman D, Shaw L, Xiao TD. Development of grain-tolerant nanostructured Al2O3–TiO2 coatings. Surf Coat Technol. 2001;146–147:48–54.
17. Raghavendra CR, Jhansilakshmi M. Tribological behaviour of plasma sprayed Ni–Cr/nano-Al2O3 composite coatings on AA6061. Mater Today Proc. 2021;44:931–936.
18. Pattnayak A, Madhu N, Panda AK, Paswan MK, Dash AK. Tribological behaviour of Al2O3–CeO2–graphene-oxide HVOF coatings. Surf Coat Technol. 2021;425:127696.
19. Elwith J, Suyamburajan V, Lakshmanan P. Statistical analysis of wear and friction behaviour on plasma sprayed nano Al2O3–TiO2–AISI 1020 steel coatings using definitive screening design. Int J Interact Des Manuf. 2025;19:5999–6018.
20. Toma D, Brandl W, Marginean G. Wear and corrosion behaviour of thermally sprayed cermet coatings. Surf Coat Technol. 2001;138(2–3):149–158.
21. Anbuchezhiyan, G., Saravanan, R., Pugazhenthi, R., Palani, K., & Mamidi, V. K. (2022). Influence of coated electrode in nanopowder mixed EDM of Al–Zn–Mg–Si3N4 composite. Advances in Materials Science and Engineering, 2022(1), 9539790.
22. Singh G, Kaur M. Wear and corrosion behaviour of plasma sprayed NiCrSiFeBC–WC–Co coatings. Mater Res Express. 2019;6(9):096577.
23. Jones BA, Nachtsheim CJ. A class of three-level designs for definitive screening in the presence of second-order effects. J Qual Technol. 2011;43(1):1–15.

24. Kumar, S. D., Pugazhenthi, R., Ajith Arul Danial, S., & Swaminathan, G. (2021, October). Optimization of Dissimilar aluminum alloy by Friction stir welding Process Control variables with Multiple Objectives. In Journal of Physics: Conference Series (Vol. 2040, No. 1, p. 012042). IOP Publishing.
25. ASTM G102-89(2015)e1. Standard Practice for Calculation of Corrosion Rates and Related Information from Electrochemical Measurements. West Conshohocken (PA): ASTM International; 2015.
26. ASTM G59-97(2020). Standard Test Method for Conducting Potentiodynamic Polarization Resistance Measurements. West Conshohocken (PA): ASTM International; 2020.
27. Scaria, C. T., Pugazhenthi, R., Daniel, A. A., & Santhosh, K. (2022). Mechanical and wear studies on AA7075/nano TiC/graphite hybrid composites for tribological applications. Advances in Materials Science and Engineering, 2022(1), 5320363.
28. Macdonald DD. Reflections on the history of electrochemical impedance spectroscopy. Electrochim Acta. 2006;51(8–9):1376–1388.
29. Liu C, Bi Q, Leyland A, Matthews A. An electrochemical impedance spectroscopy study of the corrosion behaviour of PVD coated steels. Corros Sci. 2003;45(6):1243–1256.
30. Berndt CC, Lin CK. Measurement of adhesion for thermally sprayed coatings. J Adhes Sci Technol. 1993;7(12):1235–1264.